

# 1 Generative AI for image reconstruction in Intensity Interferometry: a first attempt

2 KM NITU RAI,<sup>1,2</sup> YURI VAN DER BURG,<sup>3</sup> SOUMEN BASAK,<sup>1</sup> PRASENJIT SAHA,<sup>3</sup> AND SUBRATA SARANGI<sup>4,5</sup>

3 <sup>1</sup>School of Physics, Indian Institute of Science Education and Research Thiruvananthapuram, Maruthamala PO, Vithura,  
4 Thiruvananthapuram 695551, Kerala, India.

5 <sup>2</sup>Aryabhatta Research Institute of Observational Sciences, Manora Peak, Nainital 263129, India.

6 <sup>3</sup>Physik-Institut, University of Zurich, Winterthurerstrasse 190, 8057 Zurich, Switzerland.

7 <sup>4</sup>School of Applied Sciences, Centurion University of Technology and Management, Odisha-752050, India.

8 <sup>5</sup>Visiting Associate, Inter-University Centre for Astronomy and Astrophysics, Post Bag 4, Ganeshkhind, Pune 411 007, Maharashtra,  
9 India.

## ABSTRACT

In the last few years Intensity Interferometry (II) has made significant strides in achieving high-precision resolution of stellar objects at optical wavelengths. Despite these advancements, phase retrieval remains a major challenge due to the nature of photon correlation. This paper explores the application of a conditional Generative Adversarial Network (cGAN) to tackle the problem of image reconstruction in Intensity Interferometry. This approach II. This method successfully reconstructs the shape, size, and brightness distribution of a simulated fast-rotating star from sparsely sampled stars based on a sparsely sampled spatial power spectrum of the source, corresponding to H with four telescopes obtained from a hypothetical ground-based II facility composed of four Imaging Atmospheric Cherenkov Telescopes (IACTs). Although this particular example could also be addressed using parameter fitting, the results suggest that with larger arrays much more complicated systems could be reconstructed by applying machine-learning techniques to II.

## 22 1. INTRODUCTION

23 Humans instinctively feel a relationship with the stars. One of the primary scientific projects of humanity is to figure out what the stars are and how do they do what they do. The first obvious step in this project, beyond measuring their global parameters like diameter, mass, orbital and astrometric elements, is to obtain images of the stars with all details of the stellar surfaces. In case of the Sun, this is done routinely by observatories and Sun-observation satellites. But such a routine still remains a challenge even for the  $\alpha$ -Centauri system, our nearest stellar neighbour. The objective is to achieve capability of high fidelity image reconstruction of distant stars. Two interferometry based techniques, namely, Michelson Interferometry (MI) or Intensity Interferometry (II) was first reported have emerged during the last century to address this objective. A discussion of the development of these two approaches and comparison of their respective merits and challenges can be found in (?). The work reported here presents the results of a first effort at applying a Conditional Generative Adversarial (neural) Network (cGAN) to image reconstruction of a fast rotator using its simulated II observations.

45 The foundational basis of II stems from the  
46 pioneering experiments and theoretical investigations  
47 carried out initially by Hanbury Brown and  
48 Twiss (HBT) during the 1950s (?) as a (???)  
49 and, later, by (?) and others. The correlation  
50 between photons (called the widely referred  
51 to as the “new type of interferometry” HBT  
52 effect” to measure stellar parameters such as angular diameter, or  
53 measured by a pair of photon detectors in two partially  
54 coherent beams of light was reported in 1956 ?. ?  
55 present a recent variant of this experiment, carried out  
56 with pseudo-thermal light. The HBT Effect and the  
57 related theoretical investigations laid the foundation for  
58 Quantum Optics (for textbook treatments see ??) the  
59 modern field of Quantum Optics.

60 5pt By the 1970s, with stellar parameter measurements of 32 stars  
61 Brown and his collaborators (?) at the historic Narrabri Stellar Interferometer, the creation and installation of the historic II facility  
62 at Narrabri, Australia, and reported the measurement  
63 of angular diameters of 32 stars and a few multiple  
64 star-systems (?). Soon after this work, however,  
65 II observations of stars was stalled for over four  
66 decades due to the unavailability of sensitive limits  
67 of the then available photon detectors and  
68 advanced data analysis equipment.

5pt More recently data processing equipment. With gradual mitigation of such issues, proposals to utilize Imaging Atmospheric Cherenkov Telescope (IACT) facilities for conducting II observations of stars have emerged(????). It has been demonstrated that such observations could be a secondary science application of these facilities during moonlit nights. SII observations at VERITAS, MAGIC, and H.E.S.S. are now being reported (e.g., ???). This approach has the potential to enhance the scientific output of existing IACT facilities, and especially of the upcoming Cherenkov Telescope Array Observatory (CTAO). SH observations at VERITAS, MAGIC, and HESS are now being reshaped (and, ???). Simulations (noted ??) brightness-argued Simulations are then assessed using moments.

5pt Beyond measuring stellar diameters and other parameters of star systems, a fundamental goal of optical astronomy is to improve the quality of the images. One of the main thrusts of these efforts has been to measure the average global parameters of stars and star systems. High-fidelity imagery, however, would transcend the measurement of global and average stellar parameters, such as angular diameters, binary separations, and orbital characteristics, which offer only an integrated view of the star or star system as a whole. Such imaging capabilities promise direct insights into the dynamic surface phenomena, including limb darkening, convection cells, granulation, star spots, oblateness and gravity darkening in rapid rotators and atmospheric structures, akin to the detailed observations routinely conducted on our own Sun.

As it stands today, studies grappling various issues of image reconstruction are being reported (????). MI-based image reconstruction has made substantial progress in this area with efforts at generating reconstructed images of stars like Betelgeuse (?) and AZ Cyg (?). On the other hand, II-based methods are at a nascent stage. Some recent publications ?? have demonstrated, through outdoor experiments, imaging millimeter-scale targets at 1.36 km with a resolution 14 times better than a single telescope's diffraction limit. A "flexible computational algorithm" reconstructs images from intensity correlations, overcoming atmospheric turbulence and optical imperfections.

We report here, the results of our attempt – the first of its kind – to construct the gravity-darkened sky-image of fast rotating stars consistent with their respective simulated ground-based II-observations using a cGAN neural network architecture. Image reconstruction in gravity-darkened fast-rotating stars has long been examined using various methods in MI (????????). Recently photosphere oblateness of  $\gamma$ -Cassiopeia

(?) has been measured at the VERITAS observatory using II. These results put our work in context, and our work presented here is a natural next step especially of the work by ?. We implement a cGAN model (?) to reconstruct images of fast-rotating stars by causing off-the-shelf simulated Intensity Interferograms observations based on the sky-intensity distributions as input data for training, testing, and validation. We consider an array of four Imaging Cherenkov Telescopes (IACTs) whose relative positions approximately mimic those at VERITAS and simulate observations of a set of synthetically generated fast-rotating stars. The image predicted by the trained cGAN shows promising results in reconstructing the star's brightness distribution (noted ??). Simulations (noted ??) brightness-argued Simulations are then assessed using moments.

This paper is organized as follows. The next section discusses briefly the past efforts at image reconstruction on II, followed by the section on a discussion of II, focusing on its signal and noise characteristics for fast-rotating stars along the Earth's rotation. The following section introduces the cGAN formulation and its structure. The fifth section details the parameter selection for training the network for image reconstruction. The sixth section presents the results of the phase of the interferometric signal is lost. Since a complete reconstruction is not possible, we present the results both visually and via image moments. Finally, the paper concludes with a discussion of the overall results.

5pt Several theoretical and computational approaches have been developed for phase reconstruction with II have been proposed in intensity interferometry (II).

## 2. PAST EFFORTS AT IMAGE RECONSTRUCTION RELEVANT TO INTENSITY INTERFEROMETRY

Several approaches have been developed for phase reconstruction with II have been proposed in intensity interferometry (II). ? introduced the concept of triple-intensity correlation, which ? subsequently applied in an experiment to observe scattering by ? to microscopic systems and extended by ??? to measure stellar diameters and phases, though limited by low signal-to-noise ratio (SNR) remained a significant challenge for this approach.

5pt ? suggested an iterative method to determine the phase from images. ? proposed an iterative phase retrieval method using image and diffraction plane pictures. This method relies on accurate initial estimates and is vulnerable to slow convergence or divergence. ? improved this with the Hybrid Input-Output algorithm that incorporates feedback mechanisms to improve convergence.

5pt Later, ? proposed an alternative method that utilizes the Cauchy-Riemann relations to reconstruct for 1-D

173 images. They also extended the approach to and 2-D  
 174 images across a range of signal-to-noise (SNR) values. This al  
 175 reconstruction, applied to simulated data of stellar objects usir  
 176 data with Imaging Cherenkov Telescope Arrays  
 177 (IACTs) with a large number of telescopes (??). However, tl  
 178 but faced computational complexity for higher dimen-  
 179 sions.

180 5pt, suggested a flexible iterative Regularization method tl  
 181 introduced a regularized iterative method incorporating  
 182 priors (e.g., sparsity, smoothness, or non-negativity) to reduce  
 183 ) to mitigate noise and ill-posedness, though  
 184 challenged by parameter tuning and initial guess  
 185 sensitivity. The Transport-of-Intensity Equation  
 186 (TIE) method is a non-interferometric technique first ,  
 187 proposed by ? that relates the intensity variations along the optical axis to the phase of the optical fields. This method enables ph  
 188 retrieves phase from intensity variations  
 189 across planes; ? solved TIE as a Poisson  
 190 equation using a maximum intensity assumption", thereby converting the TIE into a Poisson equation which in turn the weight of the field. Moreover, it has been explored hybrid  
 191 while ? combined TIE with the Transport of Phase  
 192 Equation (TPE). These approaches leverage the strengths of both equations to improve phase retrieval accuracy. This method is  
 193 improved accuracy across arbitrary apertures and non-  
 194 uniform illumination, and accommodates inhomogeneous boundary conditions. It guarantees convergence, although the speed of  
 195 convergence dependent on initial guesses and boundary  
 196 conditions.

197 With non-linearity built into their architecture, artificial  
 198 neural networks (ANNs) empowered by deep learning  
 199 methods are promising for exploring the task of re-  
 200 constructing images of stellar objects from ground-based  
 201 observations. Convolutional Neural Networks (CNNs),  
 202 with their specialized architecture for processing two-  
 203 dimensional datasets, are a natural choice for image  
 204 processing tasks. In astronomical image reconstruction  
 205 projects, a common challenge is that the interferometric  
 206 data are typically undersampled as well as noisy. There-  
 207 fore, the CNN architectures and deep learning methods  
 208 employed must be capable of reliably learning both the  
 209 global context of the training dataset and the local fea-  
 210 tures within it. Among the various CNN architectures,  
 211 U-Net models (?) have proven successful in such tasks.

212 Furthermore, given that achieving a high signal-to-  
 213 noise ratio (SNR) is often challenging in astronomical  
 214 datasets, it is immensely beneficial if additional data can  
 215 be generated using the available information from the  
 216 observed sky density distribution and ground-based ob-  
 217 servations (II data, in our case) of the sources under in-  
 218 vestigation. Generative Adversarial Networks (GANs),  
 219 introduced by ?, have been successful in such data aug-  
 220mentation tasks. Conditional GAN (cGAN) architec-  
 221 tures, proposed by ? and applied to a wide variety of  
 222 datasets by ?, leverage additional information about the  
 223 images in the training datasets and have demonstrated

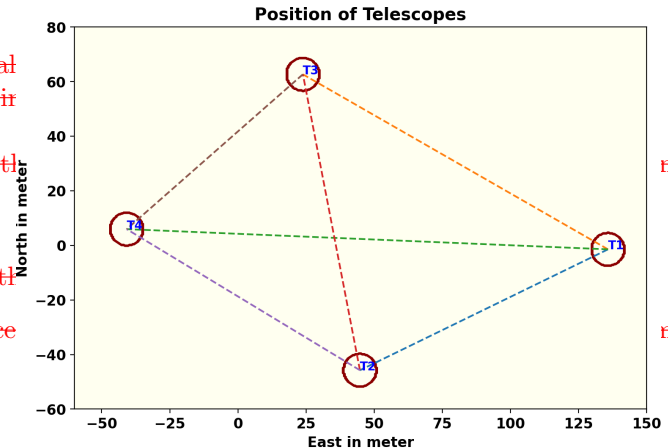


Figure 1. The telescope configuration A schematic representation of a hypothetical observation facility with similar properties each an the array of four Cherenkov Telescopes (IACTs) whose relative positions approximately mimic those at VERITAS. This array is used to simulate in boundary conditions. It guarantees convergence, although the speed of data types.

In the astrophysical context, ? employed a GAN model to recover features—such as spiral arms, central bulges, and disk structures of galaxies—from noise-affected images. ? developed and customized a Deep Convolutional GAN, dubbed “CosmoGAN”, capable of generating high-fidelity weak-lensing convergence maps of dark matter distribution that statistically reproduce real weak lensing structures. ? have successfully generated credible images of planets, nebulae, and galaxies using “lightweight” and “physics-uninformed” GANs to produce synthetic images of celestial bodies. They also generated a “Hubble Deep Field-inspired” wide-view simulation of the universe.

5pt In this paper, we propose a conditional Generative Adversarial

### 3. INTENSITY INTERFEROMETRY (II) WITH IACT ARRAYS

5pt This paper is organized as follows. The next section discusses

### 4. INTENSITY INTERFEROMETRY (II) WITH IACT ARRAYS

This section presents a brief conceptual overview of how an array of telescopes is used to perform II observations, and explains the Signal-to-Noise Ratio (SNR) from these measurements. Absolute value of the two-dimensional Fast Fourier Transform of the

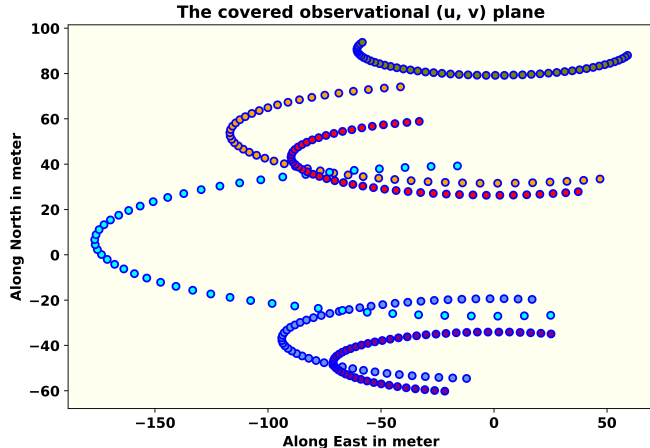


**Figure 2.** The tracks of the baselines due to Earth rotation (described in sec. 3.3) provided by the hypothetical observation facility of four telescopes arranged in fig. 1 for one night of observation. The number of baselines scales as square of number of telescopes in the array thus leading to greater coverage of the observational plane and better image reconstruction prospects.

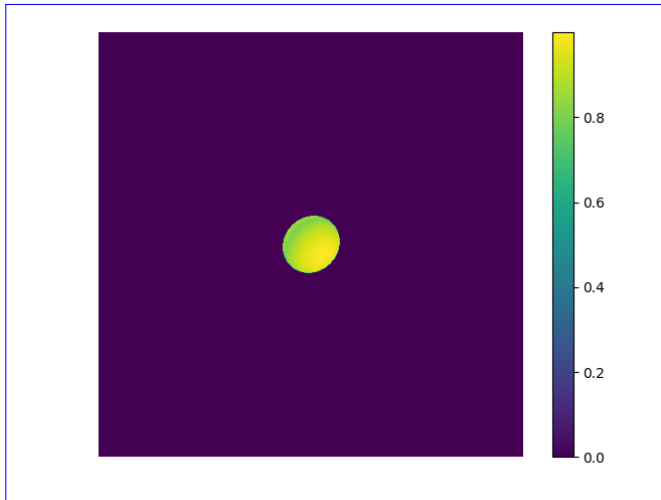


**Figure 3.** This figure shows one of the simulated fast rotating stars (FRS). The brightness is highest at the poles and there is gravitational: gravity darkening visible along the equator. A total of 31460 such images of FRS with different parameter values have been generated to train the model.

### 3.1. The signal for II

As a simple example, let us consider a pair of IACTs pointed at a star. Suppose the two telescopes simultaneously measure the intensity of radiation  $I_1(t)$  and  $I_2(t)$ , respectively. The signals from these detectors are cross-correlated and averaged over time, yielding the second order ( $n = 2$ ) correlation of these intensities as (cf. ??)

$$g^{(2)} = \frac{\langle I_1(t) \cdot I_2(t + \tau) \rangle}{\langle I_1(t) \rangle \cdot \langle I_2(t) \rangle} \quad (1)$$

where  $\tau$  is the time delay between the telescopes. For spatially coherent and randomly polarized light, Eq. (1) reduces to the relation (sometimes called the Siegert relation, see e.g., ?).

$$g^{(2)} = 1 + \frac{\Delta f}{\Delta \nu} |V_{12}|^2 \quad (2)$$

where  $\Delta f$  is the electronic bandwidth of the photon detectors which measure the intensities and  $\Delta \nu$  is the frequency bandwidth of the filters employed in the telescopes to observe the star. Values of  $\Delta \nu \sim 1$  THz and  $\Delta f \sim 1$  GHz are typical of recent work. In Eq. (2),  $V_{12}$ , referred to as the complex visibility function, is the Fourier transform of the source brightness distribution.

For a uniform disk source representing the star, it is given by

$$V_{12} = 2 \frac{J_1(\pi \theta_D b)}{(\pi \theta_D b)}$$

where  $\theta_D$  is the angular diameter of the star and  $b$  is the radial coordinate. This contains information about the star's angular diameter. However, the phase information is lost since we measure only the absolute value  $|V_{12}|^2$ . In observational astronomy, the correlation is often expressed in terms of the normalized contrast, given by:

$$c = \frac{\langle (I_1(t) - \langle I_1 \rangle) \cdot (I_2(t + \tau) - \langle I_2 \rangle) \rangle}{\langle I_1(t) \rangle \cdot \langle I_2(t) \rangle} = g^{(2)} - 1$$

where,  $\langle I_1 \rangle$  and  $\langle I_2 \rangle$  denote the mean intensities from the two telescopes.

$$c = g^{(2)} - 1 = \frac{\Delta f}{\Delta \nu} |V_{12}|^2 \quad (3)$$

with  $|V_{12}|^2$  being a function of baseline  $b = \sqrt{u^2 + v^2}$  on the observational plane  $(u, v)$ . This implies the strength of the signal would be enhanced if a larger number of baselines or pairs of telescopes are employed.

### 3.2. The Signal-to-Noise Ratio for II

The primary purpose of IACTs is to study high-energy gamma rays (with energy  $E \geq 30$  GeV) arriving from cosmic sources, entering the Earth's atmosphere, and initiating Cherenkov showers in the upper atmosphere due to multiple scattering. These telescopes feature an array of mirrors that focus light onto a received set of photomultiplier tubes (PMTs, see e.g., ?) with appropriate specifications needed for II observations. In the simulation model adopted here, we consider a set of four IACTs, each with similar properties. The positional configuration of these IACTs is shown in Fig. 1. The optical signal directed to a PMT is filtered using a spectral filter with a chosen mean observational wavelength  $\lambda$  and corresponding bandpass  $\Delta\lambda$ . The use of filters not only reduces background noise but also improves the

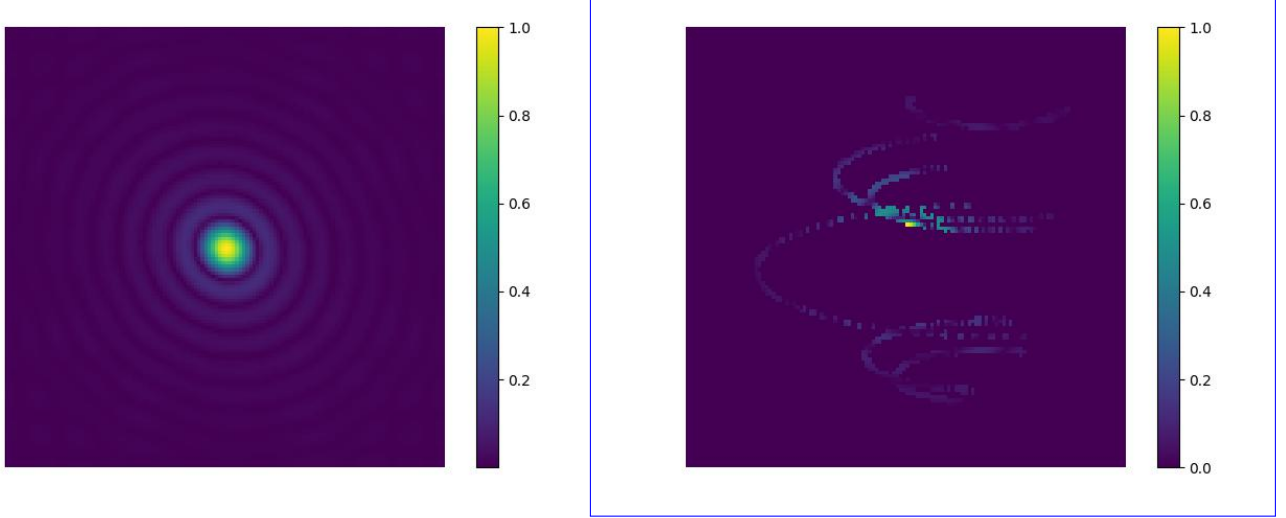


**Figure 4.** Absolute The left panel shows the absolute value of the two-dimensional Fast Fourier Transform of the source depicted in Fig. 3 in linear scale (left panel) and logarithmic scale (right panel). These figures represent It represents the intensity interferometric  $(u, v)$  plane image of the source that would be obtained by an infinite number of baselines (or an infinite number of telescopes observing the source). Both The right panel shows the linear absolute value of the same source measured along the tracks shown in Fig. 2. This figure reflects the sparse nature of the signal received by a realistic finite number of telescopes and baselines sampled from the logarithmic scales full  $(u, v)$  plane signal space, as shown in the figure on the left panel. Both figures are plotted on a linear scale and normalized to the maximum intensity obtained at the centre of figures pixel value in each respective figure.

signal quality and the efficiency of the PMTs. Filtering background skylight becomes even more significant in II observations, as, currently, these are carried out during full moon nights when the primary function of the IACTs (of observing Cherenkov Showers) is rendered infeasible. It is important to note that the light from the stellar source is focused on a PMT attached with each of the telescopes during II observations.

The significance of the signal can be expressed in terms of the signal-to-noise ratio (SNR), which depends on many factors. However, most importantly, it does not depend on the optical bandwidth  $\Delta\nu$  of the radiation for a two-telescope correlation. The explanation for the independence of the SNR from  $\Delta\nu$  is provided in several works (e.g., subsection 4.1 of ?). The Signal-to-Noise is given by

$$SNR = A \cdot \alpha \cdot q \cdot n \cdot F^{-1} \cdot \sigma \cdot \sqrt{\frac{T\Delta f}{2}} \cdot |V_{12}|^2 \quad (4)$$

Here,  $A$  is the total mirror area,  $\alpha$  is the quantum efficiency of the PMTs,  $q$  is the throughput of the remaining optics, and  $n$  is the differential photon flux from the source. The excess noise factor of the PMTs is represented by  $F$ ,  $T$  denotes the observation time, and  $\sigma$  is the normalized spectral distribution of the light (including filters) (e.g., ?).

The signal ( $S$ ) and noise ( $N$ ) can be inferred using eqns. 3 and 4:

$$S = \Delta f \frac{A \cdot \alpha \cdot q \cdot n \cdot F^{-1} \cdot \sigma \cdot \sqrt{\frac{T\Delta f}{2}} \cdot |V_{12}|^2}{\Delta\nu |V_{12}|^2}$$

and

$$N = (A \cdot \alpha \cdot q \cdot n \cdot F \cdot \sigma \cdot \Delta\nu)^{-1} \sqrt{\frac{2\Delta f}{T}}.$$

While most of the parameters can be optimized with hardware, the

### 3.3. Baseline considerations

The measurement of the size of stellar objects via squared visibility depends on the distance between the telescopes, known as the baseline  $b$ .

$$|V_{12}(b)|^2 = \frac{c(b)}{c(0)} \quad (5)$$

For achieving a good SNR with a given telescope configuration, covering as much as possible of the interferometric plane is always desirable. If the source is at the zenith, the coordinates in the Fourier plane  $(u, v)$  are given by:

$$(u, v) = \frac{1}{\lambda} (b_E, b_N) \quad (6)$$

where  $b_E$  and  $b_N$  are, respectively, the baselines expressed in east and north coordinates. However, of course the sources can be anywhere on the sky, and the telescopes are stationary and may also have different relative altitudes  $b_A$  depending on the available terrain. Therefore, the In order to gather maximum possible information on the source during the observation session and to cover as much of the observational plane as possible during such

330 sessions, Earth's rotation must be taken into account to cover the maximum observational plane using  
 331 rotated baselines. For a given stellar source with declination  $\delta$  and hour-angle  $h$ , as observed by telescopes  
 332 located at latitude  $l$ , equation (7) provides the rotated  
 333 baselines for a given pair of telescopes (see e.g., eqs. 8–10  
 334 from ?) with the  $R$ -matrices representing the respective  
 335 rotation operations.

$$338 \begin{pmatrix} u \\ v \\ w \end{pmatrix} = R_x(\delta) \cdot R_y(h) \cdot R_x(-l) \begin{pmatrix} b_E \\ b_N \\ b_A \end{pmatrix} \quad (7)$$

339 Fig. 2 shows the track of six baselines generated from  
 340 the telescopes (Fig. 1) due to the Earth's rotation. Since  
 341 every pair of telescopes traces an ellipse in the Fourier  
 342 plane, the total number of ellipses scales as

$$343 \mathcal{N} = \frac{1}{2} N_T \cdot (N_T - 1) \quad (8)$$

344 where  $N_T$  is the number of telescopes considered. As  
 345 the number of baselines increases non-linearly, Intensity  
 346 Interferometry (II) benefits greatly from a large number  
 347 of telescopes. The CTAO can offer many more baselines — ?  
 348 considered the telescope configurations then being  
 349 planned and showed how it would provide a dense  
 350 coverage of the interference plane.

### 351 3.4. A Fictitious Fast Rotating Star: Our Test Case

352 In our work presented here, we simulate a single attempt  
 353 image reconstruction of a fast-rotating star to test image reconstruction using a GAN using its  
 354 simulated Intensity Interferometric observation in a cGAN architecture. Fast-rotating stars are important  
 355 test cases for understanding various astrophysical  
 356 processes, including stellar evolution, internal structure,  
 357 and dynamical behaviour over time. Fast rotation  
 358 causes stars to adopt an oblate shape, flattening  
 359 at the poles and bulging at the equator due to the  
 360 stronger centrifugal force (e.g., ??). Fig. 3 shows an  
 361 image qualitatively representing a fictitious fast-rotating  
 362 star, with brightness (and, therefore, the effective  
 363 surface temperature) distributed across its surface.  
 364 The brightness (effective temperature) is highest at  
 365 the poles and lowest at the equator, a phenomenon  
 366 known as gravity darkening (?). This effect First  
 367 direct interferometric detection of stellar photospheric  
 368 oblateness (of Altair) was pioneered by ? using the  
 369 Palomar Testbed Interferometer (PTI) and the Navy  
 370 Prototype Optical Interferometer (NPOI). Gravity  
 371 darkening due to fast rotation was first observed  
 372 through interferometric and spectroscopic data from  
 373 the CHARA Array for the fast-rotating star Regulus

376 ? Fast-rotating stars are important test cases for understanding va

377 As pointed out earlier, these two pieces of work,  
 378 all using Michelson Interferometry, make a subset of  
 379 several others (??????). The first observation of  
 380 photospheric oblateness (of  $\gamma$  Cassiopeiae or  $\gamma$ -Cas)  
 381 using Intensity Interferometry (II) has been recently  
 382 carried out at VERITAS observatory and is reported by  
 383 ?. Reportage of such observations of other  $\gamma$ -Cas like  
 384 targets and other class of FRS by Cherenkov Telescope  
 385 arrays, such as the MAGIC array, are expected by  
 386 2026. In addition, observation and measurement of  
 387 gravity darkening using II is the natural next step  
 388 and is yet to be reported. In this context, our  
 389 work of reconstructing the image of FRSs from their  
 390 II-simulated observations using cGAN is an attempt at  
 391 solving this inverse problem along with mitigation of  
 392 loss of phase information in II.

393 5pt **Intensity Interferometry** II counts the photons arriving at the telescopes from the stellar object. The correlation of these photon arrivals at the telescopes yields the squared visibility Eq. (5), as explained in subsection 3.1. **The left panel of fig. 4** shows the signal from the source shown in Fig. 3 using II, displayed in both linear and logarithmic scales. Point on linear scales. A point to note here is that this figure represents the signal from the source that would be recorded by an infinite number of baselines provided by an infinite number of telescopes on the interferometric plane. In practice, only a small part of this information is available (as seen in right panel of Fig. ??), because one has a finite number of baselines corresponding to the finite number  $N_T$  of telescopes at our disposal and a limited observation schedule. We have simulated the II observation of the fictitious star by four telescopes a hypothetical observation facility having an array of four IACTs with their relative positions approximating those at VERITAS (correlated with baselines as seen in Fig. 1) over one night. Using this modest amount of signal from one night's observation, we have trained a cGAN to construct the image of the source.

## 4. GENERATIVE ADVERSARIAL NETWORKS

418 Generative Adversarial Networks (GANs) were introduced by ?. The underlying concept is straightforward: it A  
 419 GAN model involves two competing networks. The first network , k  
 420 neural network models, referred to as the Generator  
 421 , produces new images based on an input image. These will be refe

422 5pt Through the alternating training of these networks, the gener  
 423  $\min_G \max_D V(D, G) = \mathbb{E}_{x \sim p_{\text{data}}(x)} [\log D(x)] - \mathbb{E}_{z \sim p_z(z)} [\log (1 - D(G(z)))]$

424 where  $V(D, G)$  denotes the value function of the min-max game.

425 5pt The objective is to learn the Generator's distribution,  $p_G$ , over  
 426 the Discriminator. These two networks engage in



**Figure 5.** ~~Merged~~ An illustrative example of the input used for training the cGAN model. The picture on the left shows the source image, which ~~includes~~ serves as the original ground truth or the real data ( $x$ ), as mentioned in the Flow Diagram (Fig.6 discussed later during the training). The picture on the right represents the simulated II observation pattern of the source (on the left) using a hypothetical observation facility having as array of four IACTs (see Fig. 1) and the sparsely sampled Fourier plane tracks of the six telescope baselines (see Fig. It is exactly what 2) generated by these four IACTs due to Earth's rotation during the observation session. This pattern referred to as  $y$ , in the Flow Diagram (Fig.6 discussed later) forms the "condition" during the training to which the GAN receives model has to conform. The grey scale Salt-and-pepper noise is added to this pattern for enhancing the robustness of the figure cGAN model. Together, these images form a training pair, where the GAN learns to reconstruct a predicted image (modeling of observed signal) similar to ground truth (left) from the noisy baseline signal (right). The grayscale in both images is normalized to the brightest pixel in the image.

a zero-sum “Minimax” game, as in Game Theory. Given a real data set  $\{x_i\}$  (for example, a set of real images) drawn from some unknown distribution  $P_{\text{data}}(x)$  generated by some unknown or ill-understood process, the objective here is to generate a new set (of images) whose probability distribution should match  $P_{\text{data}}(x)$  as closely as possible. During the training of the two models, the Generator samples a latent variable  $z$  from a known prior distribution  $P_z(z)$  (e.g., the Normal Distribution) and produces a synthetic sample  $G(z)$  to start with and, subsequently, based on updates received from the Discriminator as its training progresses. The Discriminator, being a probabilistic binary classifier receives either a real data sample  $x$ . We begin with input noise variables  $p_z(z)$  and employ two perceptrons,  $G(z; \theta_G)$  and  $D(x; \theta_D)$ , or a generated sample  $G(z)$ , and outputs a probability that the input is real. The Discriminator aims to maximise its classification accuracy, while the Generator aims to fool it by trying to minimize it. The training of these two networks proceeds alternately leading to the optimization of the adversarial loss function  $L(D, G)$

given by

$$\begin{aligned} L(D, G) &= \min_G \max_D V(D, G) \\ &= \mathbb{E}_{x \sim p_{\text{data}}(x)} [\log D(x)] \\ &\quad + \mathbb{E}_{z \sim p_z(z)} [\log (1 - D(G(z)))] . \end{aligned} \quad (9)$$

The two neural networks  $G(z) \equiv G(z; \theta_G)$  and  $D(x) \equiv D(x; \theta_D)$  are parameterized by  $\theta_i$  with  $i = G$  or  $D$  respectively. Here,  $G(z)$  is a differentiable function. During its training, the Generator generates the differentiable function  $x_{\text{gen}} \equiv G(z)$  that maps  $z$  to the data space  $x$ , while  $D(x; \theta_D)$  or generates its own distribution  $p_G(x_{\text{gen}})$  and through the training episodes, specifically by iteratively updating its parameters  $\theta_G$ , aligns this distribution with the distribution of real data  $p_{\text{data}}(x)$ . The training data set provided to the Discriminator is constructed by mixing real data points  $x$  and generated data points  $x_{\text{gen}}$  in equal ratio. The Discriminator generates the function  $D(x)$  that represents the probability that  $x$  originates from real data. The Eq.(9) implies that training of the GAN model moves towards maximization of the expectation of  $D(x)$ . Through this process, both the

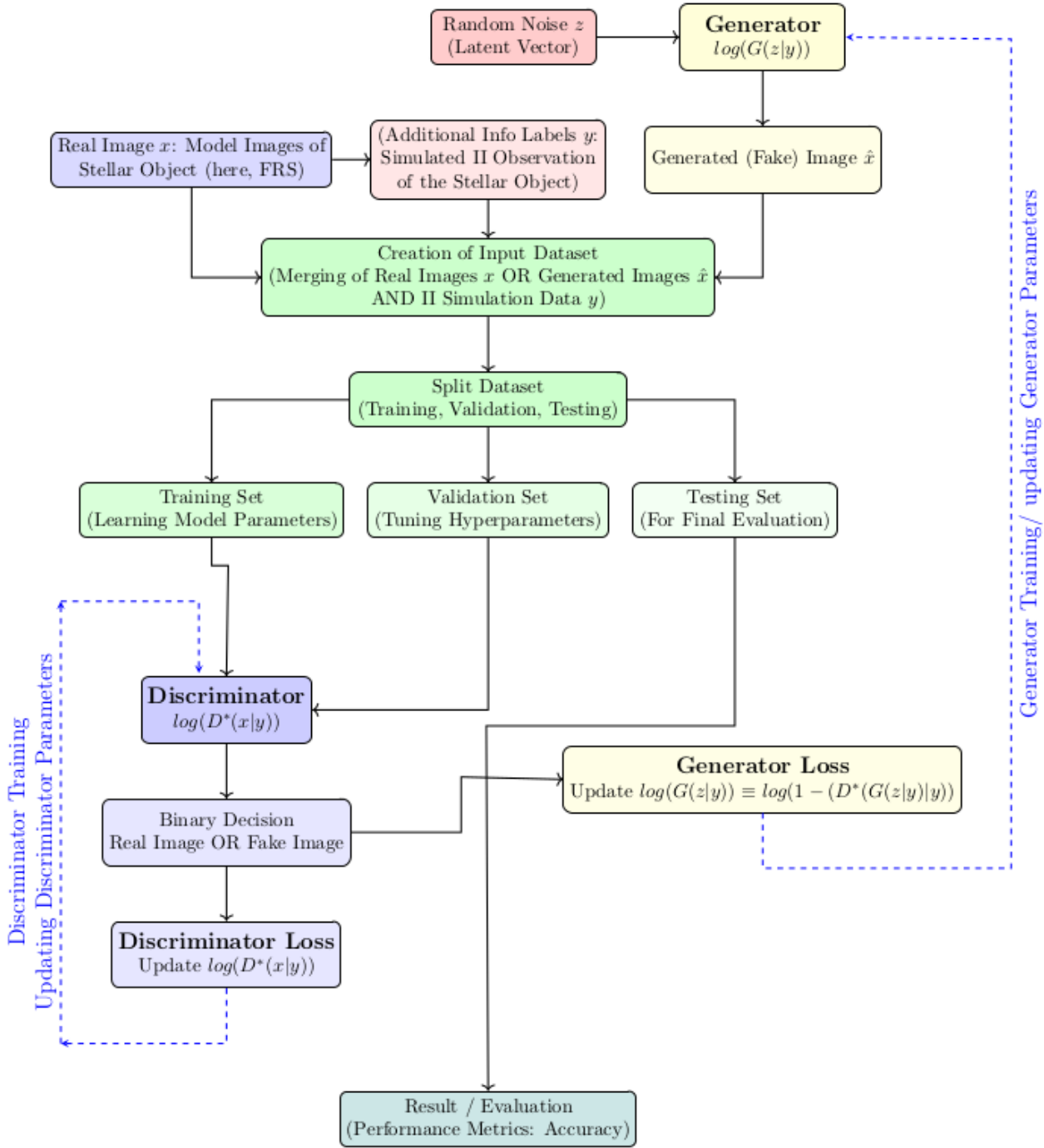


**Figure 6.** A schematic representation of the features of a cGAN model used in this work and the iterative process of its training, validation and testing. The process constitutes four broad stages: (1) choice of an appropriate GAN architecture including both the Discriminator and the Generator losses for three different learning rates (not shown in this figure) (2) preparation of the Training, Validation and Testing datasets and (3) Training and Validation of the Model (4) Testing and Evaluation of the Model. The left panel stages (2), (3) and (4) are depicted in this figure. The datasets are prepared in three broad steps: (i) generating the right panel show “ground truth” images of fictitious fast-rotators  $x$ , the total discriminator loss sparse II images  $y$  used as the “condition” images in the Model and the total generator loss generated images  $z$  sampled from a Normal Distribution (Eq(i)) merging these images into individual files with  $(x|y)$  and/or  $(z|y)$  (as seen in an illustrated sample in Fig. 15(5) respectively) and generating the full dataset in this process, and finally (iii) partitioning the full dataset into Training Set, Validation Set and the Testing Set. After the iterative training of the Model and its validation process is complete (“Nash point” of the Minimax Game is reached), but these figures indicate that higher learning rates might render the training prone to outliers Model is tested using the Testing Set and evaluated.

**5pt** Discriminator and Generator losses (left and right panels respectively) for three different kernel sizes in the convolutional layers. Here, the Effect of the Salt ( $\alpha$ ) and Pepper ( $\beta$ ) noise (explained in the text) introduced into the images. There is no significant effect of the a

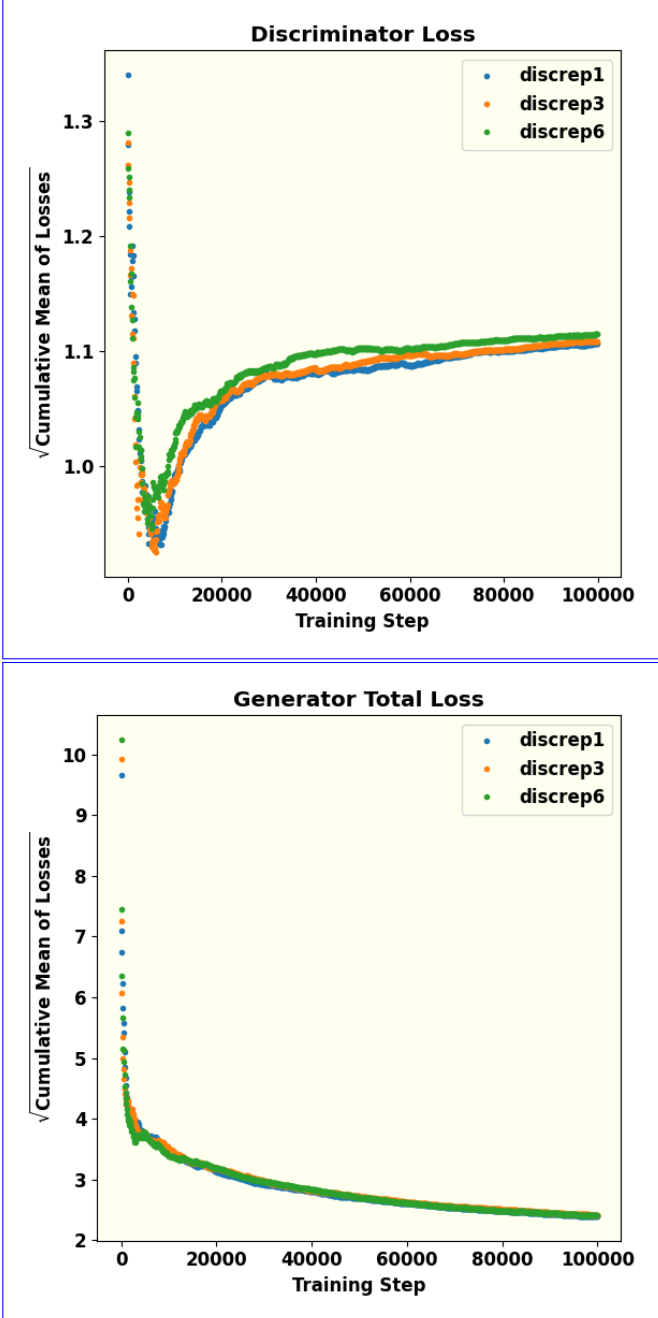


**Figure 7.** These figures show the effect of the ratio of episodes of Discriminator training per every episode of Generator training. This hyperparameter is termed Discriminator repetition or Disc(discrep) in the figures. The square root of the cumulative mean of the losses are plotted against the training steps for 3 values of this ratio. Understandably, this ratio has a higher impact on the Discriminator loss than on the Generator loss. The left and Equal number of episodes of training produces minimum cumulative loss of the right panel show this effect on Discriminator. The dip in the Discriminator loss during the initial phases of its training can be interpreted as its early success in detecting “fake” (or generated) images because of a poorly trained Generator. With gradual training of the Generator, the success rate of the Discriminator decreases and eventually approaches saturation with equal probability of being successful in telling “fake” from real. The continual decrease and eventual saturation of the Generator loss respectively is a result of its training to generate better images with increasing number of steps.

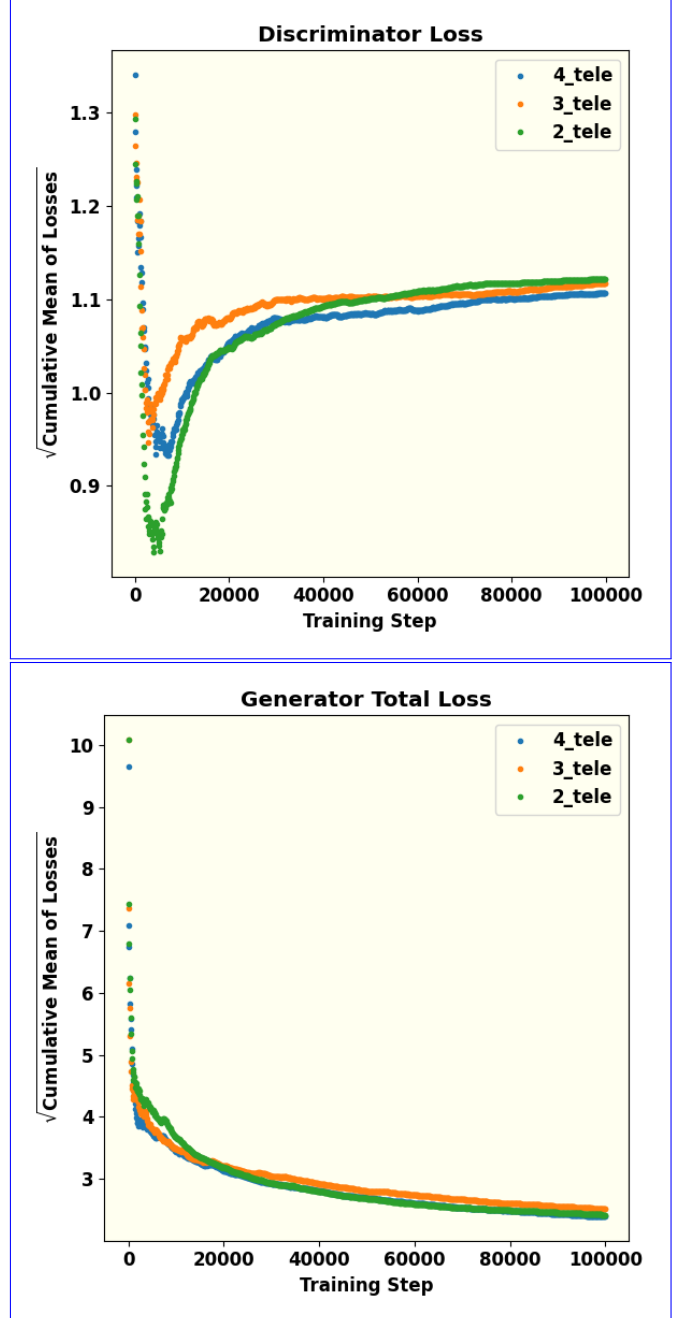


**Figure 8.** The square root of cumulative mean of Discriminator and Generator loss for different numbers of telescopes. The number of telescopes is also another hyperparameter that has a very significant impact on the model performance. If there are only two telescopes, both Discriminator and Generator are not trained smoothly. The result of four telescopes is a lot better because the cumulative mean of loss functions change only slightly is smaller compare to other parameters. For the same reasons as explained in Fig.(7), we observe initial dip and eventual saturation of the Discriminator loss and continual decrease and eventual saturation of the Generator loss with increasing training steps.

468 parameters  $\theta_G$  and  $\theta_D$  are optimized such that  $p_G(x_{gen})$   
 469 gets maximally aligned with  $p_{data}(x)$ .

470 For a given fixed Generator  $G(z)$ , the problem can be  
 471 reformulated as:

$$\max_D V(D, G) = \mathbb{E}_{x \sim p_{data}} [\log D_G^*(x)] + \mathbb{E}_{x \sim p_G} [\log (1 - D_G^*(x))] \quad (10)$$

473 where  $D_G^*$  denotes the optimum of the discriminator  
 474 for a given fixed generator, as shown. As seen in  
 475 equation (4). It can be demonstrated that the global  
 476 optimum of equation (10) is achieved if and only if  
 477  $p_G = p_{data}$ . Furthermore, if both  $G$  and  $D$  are allowed  
 478 to reach their respective optima, then  $p_G$  – the so called  
 479 Nash point of the Minimax game –  $p_G$  converges to  $p_{data}$ .

$$D_G^*(x) = \frac{p_{data}(x)}{p_{data}(x) + p_G(x_{gen})} \quad (11)$$

480 At this point, the Discriminator finds its job no better  
 481 than random guessing. A more comprehensive discussion  
 482 of the problem, including proofs, is provided in ?.

$$D_G^*(x) = \frac{p_{data}(x)}{p_{data}(x) + p_G(g)}$$

483 Subsequently, the GAN framework was extended to a  
 484 conditional model (?). In this formulation, both the Generator  
 485 new model, known as “conditional GAN”  
 486 or cGAN injects a conditioning variable  $y$   
 487 into both networks: the Generator now  
 488 generates  $G(z|y)$ , and the Discriminator  
 489 receive additional information  $y$ , and the value function of the  
 490 conditional GAN (cGAN) is expressed as

$$V(D, G) = \mathbb{E}_{x \sim p_{data}(x)} [\log D(x|y)] + \mathbb{E}_{z \sim p_z(z)} [\log (1 - D(G(z|y)|y))] \quad (12)$$

491 evaluates  $D(x|y)$ . The adversarial objective becomes  
 492

$$V(D, G) = \mathbb{E}_{x, y \sim p_{data}(x)} [\log D(x|y)] + \mathbb{E}_{z, y \sim p_z(z)} [\log (1 - D(G(z|y)|y))] \quad (12)$$

493 The conditional variable  $y$  in a cGAN can be various  
 494 additional information including images, labels or text  
 495 contextual to “ground truth” real data  $x$ . Among  
 496 various types of cGANs, Pix2Pix GAN with its  
 497 image-to-image translation design is suitable for the task  
 498 at hand. In our work, we specifically use this conditional  
 499 variable by choosing  $y$  to represent the ground-based  
 500 intensity-interferometry (II) observation patterns: the  
 501 Generator is trained to produce stellar surface images  
 502 that not only look realistic but also conform to the  
 503 measured II correlations, while the Discriminator judges  
 504 realism and consistency with the II data.

505 ? further observed that combining the cGAN  
 506 from Eq. (12) with the traditional L1 loss  $L_1(G)$

507 loss (also known as the Mean Absolute Error)  
 508 improves the results, as the Generator is en-  
 509 couraged to produce outputs closer to the  
 510 ground truth. Hence, the function that is minimized is: target  
 511 image in a pixel-wise sense. We adopt this approach  
 512 in the training of our cGAN model by including  $L_1(G)$   
 513 defined in eq.(13)

$$L_1(G) = \mathbb{E}_{x \sim p_{data}, z \sim p_z(z)} [\|x - G(z|y)\|_1]. \quad (13)$$

514 The total adversarial loss function, along with the  $L_1$   
 515 loss modulated by a hyperparameter  $\lambda$  then becomes

$$L_{tot} = \arg \min_G \max_D V(D, G) + \lambda \cdot L_1(G). \quad (14)$$

516 with the choice  $\lambda = 100$  and  $L_1(G) = \mathbb{E}_{x, y, z} \|y - G(x, z)\|_1$

517 This type of network has demonstrated remarkable  
 518 robustness across a variety of applications. For exam-  
 519 ple, it can generate colored images from grayscale inputs  
 520 based on architectural labels, transform images from day  
 521 to night, and even predict maps from satellite data. A  
 522 more extensive list of applications is provided in ?.

#### 4.1. Generator

523 As discussed above, in a GAN the Generator, a deep  
 524 neural network in itself, is responsible for produc-  
 525 ing synthetic data – in this case, images that resemble  
 526 those of a fast-rotating star. In this work, the Generator  
 527 is implemented as a U-Net convolutional network (?).  
 528 In such architectures, the image’s spatial resolution is first reduced  
 529 U-Net consists of a symmetric encoder-decoder  
 530 structure forming a characteristic “U” shape along  
 531 with skip connections: the left (contracting or  
 532 down-sampling) path, the right (expanding or  
 533 up-sampling path) and the connecting (bottle-neck)  
 534 path. The left down-sampling path repeatedly  
 535 applies  $3 \times 3$  convolutions (padded to preserve  
 536 spatial dimensions) followed by LeakyReLU  
 537 activations and strided convolution (with stride of  
 538 2) to effectively subsample the image, and a leaky version of the ReLU

539 5pt In contrast, the upsampling process uses only the standard ReLU  
 540 by progressively halving the spatial resolution while  
 541 doubling the channel depth (typically  $64 \rightarrow 128 \rightarrow$   
 542  $256 \rightarrow 512 \rightarrow 1024$ ). At the bottleneck, high-level  
 543 features are processed without further spatial reduction.  
 544 The right up-sampling path mirrors this process  
 545 using  $2 \times 2$  transposed convolutions (stride 2) for up-sampling,  
 546 halving the channel count at each level and using  
 547 ReLU as the activation function for all its layers  
 548 except the output layer. Additionally, a dropout  
 549 layer is introduced at the beginning of the upsam-  
 550 pling phase to mitigate overfitting of the Generator

model (?). Critically, long skip connections concatenate feature maps from each encoder (down-sampling) level to the corresponding decoder (up-sampling) level, directly injecting high-resolution details into the reconstruction process. This enables the network to “remember where everything is” while the deep bottleneck still provides the large receptive field needed to think globally about image structure and semantics. Besides the strided convolutions, modern variants of U-Nets used in state-of-the-art GANs incorporate residual blocks within resolution levels, and frequently add spectral normalization and self-attention at the bottleneck for improved training stability and long-range dependency modelling. These architectural choices allow our U-Net generator to simultaneously recover sharp, high-frequency details (stellar limb edges, limb-darkening profiles, gravity darkening, and rapid-rotation-induced oblateness) and enforce global coherence (overall disk morphology and physical consistency with the observed interferometric visibilities)—making it ideally suited for high-fidelity sky-image reconstruction of fast-rotating stars from sparse ground-based intensity interferometry observations.

5pt After generating images, the Generator aims to deceive the Discriminator during training, the total Generator Loss function  $L_G$  including the  $L_1$  loss defined in eq.(13) that is minimized is given by

$$L_G = -\mathbb{E}_{z \sim p_z(z)} [\log D(G(z | y) | y)] + \lambda \mathbb{E}_{x \sim p_{\text{data}}, z \sim p_z(z)} [\|x - G(z | y)\|_1]. \quad (15)$$

566 Here,

- $x$  denotes a real data sample (e.g. the “ground-truth” image; here, the Generator is considered to have reached an optimal generated fast rotator image) corresponding to condition  $y$ , the simulated II observation data.
- $z$  is a random latent vector drawn from the prior  $p_z(z)$ . Additionally, the Generator’s performance is evaluated using another metric known as the  $L_1$  loss, which is obtained by averaging over all the patch responses.
- $G(z | y)$  is the generator output (the reconstructed / synthesized image) given  $z$  and condition  $y$ .
- $D(\cdot | y)$  is the discriminator’s estimate (probability) that its input is “real,” given the same condition  $y$ .
- $\lambda$  is a hyperparameter controlling the trade-off between adversarial realism and pixel-wise fidelity (typical values depend on the problem, e.g. in pix2pix,  $\lambda = 100$ ).

## 593 4.2. Discriminator

The Discriminator is tasked with classifying the images produced by the Generator as either real or fake. It takes a real image from the dataset (often referred to as the target image for the Generator) and provides feedback to guide the Generator toward producing more accurate images. In this work, the PatchGAN model (?) is employed as the Discriminator. Unlike a traditional global classifier, PatchGAN evaluates individual patches of the image, outputting a grid of predictions rather than a single scalar value.

5pt The Discriminator’s architecture begins with an initializer that element in the grid corresponds to the “realness” of one patch of the image under examination of the Discriminator at a time. The final loss of the Discriminator is the average over all the patch responses. Evaluating the “realness” of the input image in terms of its constituent patches facilitates capture of texture/style and other high frequency components in the image. As compared to a global discriminator, it also reduces the number of parameters in the network thereby helping reduce computation cost. It also works on images with arbitrary sizes.

Prior to the down-sampling of data using PatchGAN, the input image is processed through a padding stage. Zero Padding followed by batch normalization. The purpose of Zero Padding is to prevent the loss of spatial information and to facilitate the extraction of deeper features from the down-sampled output. Batch normalization is required to stabilize the learning (loss minimization) process. PatchGAN then reduces the spatial dimensions of the images to extract localized features, ensuring the model focuses on smaller regions. In this downsampling stage, a leaky version of the Rectified Linear Unit (LeakyReLU) is applied in the convolutional layers, similar to the approach used in the Generator.

5pt Subsequently, zero padding is applied—adding rows and columns of zeros to the input image  $I$ —so that the patch of the input image represented by  $\cdot$  is “real” is evaluated through this process. The loss function  $D$  of the full input image is obtained by averaging over all the patch responses.

The effectiveness of the Discriminator is measured by its ability to distinguish between real and generated images. The loss function  $L_D$  that is optimized during the training process is given by

$$L_D = -\mathbb{E}_{x \sim p_{\text{data}}(x | y)} [\log D(x | y)] - \mathbb{E}_{z \sim p_z(z)} [\log(1 - D(G(z | y) | y))] \quad (16)$$

where the arguments of the  $D$  and  $G$  functions are as noted in the text following eq.(15). This loss is composed of two parts: one that

measures how accurately the Discriminator identifies real images. Then, the images are resized and their mean is subtracted. A two-dimensional Fast Fourier Transform, along with a Fourier shift, is applied, yielding a complex number for each pixel. Since II does not measure phase, the absolute value is calculated (as shown in Fig. 4 on both linear and logarithmic scales for v1 and v2).

The training procedure of these two components of the cGAN model can be outlined as follows:

- The discriminator  $D$  is updated by minimizing  $L_D$ , keeping  $G$  fixed (so that  $D$  becomes better at distinguishing real vs generated images).
- The generator  $G$  is updated by minimizing  $L_G$ , keeping  $D$  fixed, thus pushing  $G$  to generate images that are (a) judged “real” by  $D$ , and (b) close (in pixel-wise sense) to the ground-truth  $x$ .

## 5. NETWORK PARAMETERS

5pt Here, we discuss the parameters of the GAN architecture used for reconstructing images of stellar objects using H<sub>II</sub>. An appropriate cGAN architecture along with a set of hyperparameters was optimized by tuning. The objective of the model, as already mentioned, was to learn to faithfully reproduce a set of sky-images of fast rotators subject to the condition that those images are consistent with their simulated II observation data. We discuss below the architecture and the hyperparameters of the cGAN model used for this task. Given the adversarial nature of GANs, where the Generator and Discriminator engage in a min-max game, careful tuning of key parameters is critical to ensure that both networks are well-balanced for effective training.

### 5.1. Data Preparation

First, we simulate fast-rotating stars, generate synthetic images of rapidly rotating stars by modelling them as oblate spheroids with varying radii and an oblateness ranging between 0.5 and 1. We To incorporate the effect of gravity darkening, we also consider different viewing angles, assuming and assume a linear dependence for the effect of gravity darkening on the declination angle of each point on the stellar surface. The traced ellipses result from integrating over the source’s hour angle. For hyperparameter tuning and comparing different telescopes

Next, Salt and Pepper noise is introduced usually at a into these images; usually this is done at the rate of 0.5% of the number of pixels in the

assessments. Then, the images are resized and their mean is subtracted. A two-dimensional Fast Fourier Transform, along with a Fourier shift, is applied, yielding a complex number for each pixel. Since II does not measure phase, the absolute value is calculated (as shown in Fig. 4 on both linear and logarithmic scales for v1 and v2).

Next, sparse sampling sampling of the interferometric plane is introduced via pixel-wise multiplication between of the absolute-valued Fourier-transformed image (left panel of Fig. 4) and the sparse sampling map baseline tracks of (Fig. 2) generated by the four IACTs due to Earth rotation during the II observation. The result is a map in the Fourier plane featuring several ellipses, which is also referred to as the sparse sampling map (Fig. ?? right panel of fig. 4). This map represents the sparse sampling of the signal space (Fig. 4) corresponding to the source (Fig. 3) observed with four telescopes (Fig. 1). In essence, the right panel of fig. 4 represents the result of simulated II observation of the fictitious fast-rotator illustrated in fig. 3.

Finally, the pixels are normalized and converted we normalize the pixel values and convert them to 8-bit integers. This image represents producing an image that encodes the sparsely sampled phaseless visibility as it can be measured with, phase-free visibility measured by II. The image shown in Fig. ?? serves as the input for the GAN, which also requires the corresponding simulated (fictitious) star, which serves as the “ground truth” is processed identically to avoid any bias. These two images are merged side-by-side into a single image (as shown in Fig. 5) and used to train the GAN. This procedure is applied to all The dataset thus created is split into three parts in the proportions of 80% for training, 10% used as test data, for validation, and 10% as validation data, and the remaining 80% as training data the test set. This partition of the full dataset is indicated in the Fig. 6. In the following, we refer to these three parts as the Training Set, the Validation Set and the Testing Set respectively.

### 5.2. GAN Architecture

The GAN architecture used in this work is based on pix2pix, which utilizes a conditional GAN (cGAN) as described by Isola et al. ?, this architecture is specifically suitable for image processing and reconstruction objectives.

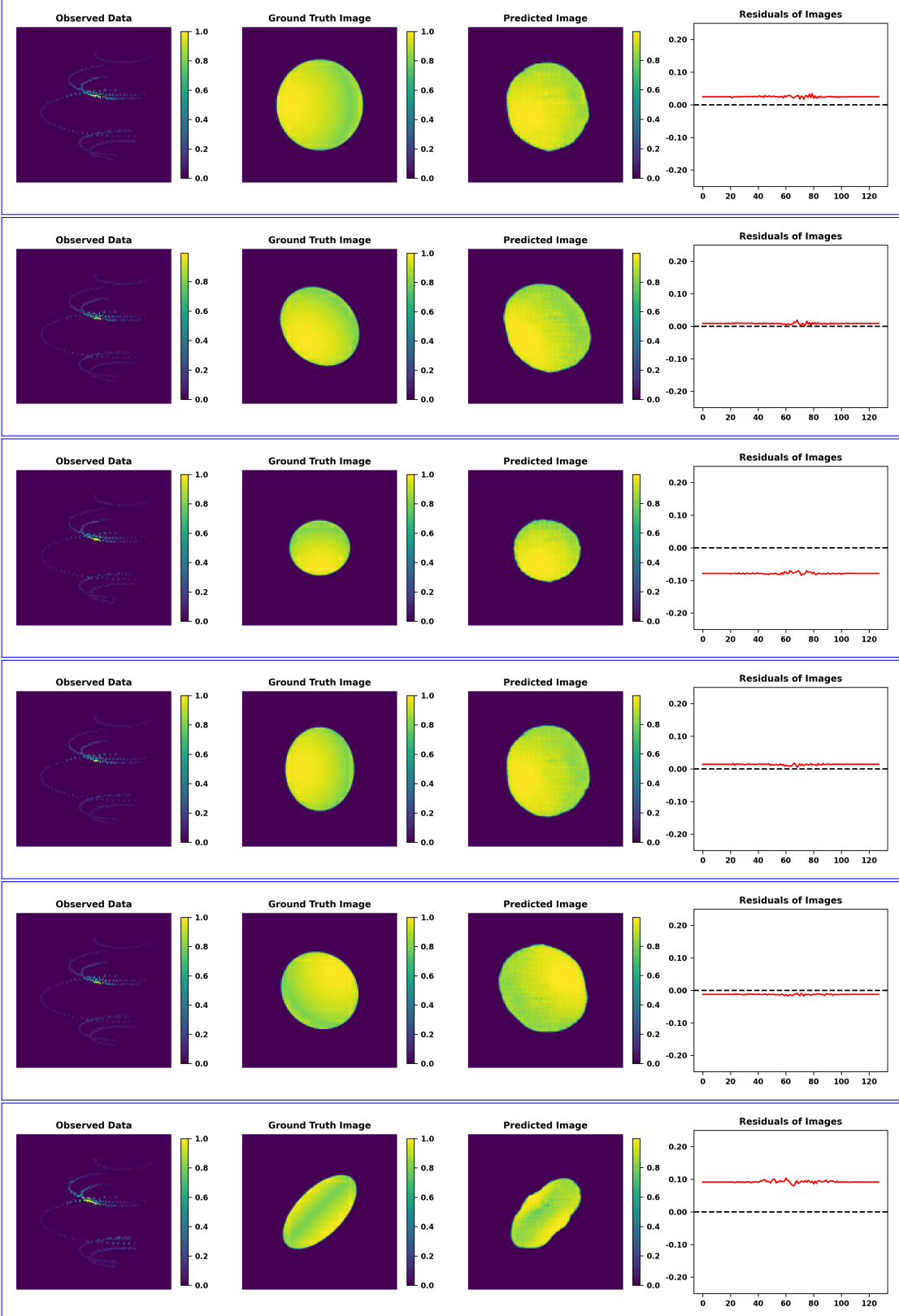


**Figure 9.** Example results of image reconstruction using the GAN-cGAN model along with the II observations simulated in this work. Each row in this figure represents the results for a hypothetical fast-rotating star. Going from The left to right in each row, the first panel represents the simulated  $(u, v)$  plane sparse II signals pattern obtained using by the six baselines (simulated observation of the star using the four IACTs illustrated in Fig.??). This image is presented, acts as the “condition” part of the data input to the trained GAN to produce a predicted imagecGAN model. The second panel is from left displays the real image of the star, also called the or ground truth, which the Discriminator uses to distinguish from the images generated by the Generator. The data generated for training, validation and testing of the cGAN model is a merge of this image and its II pattern presented in the left panel. The third panel is the reconstructed image, or the predicted image, produced by the trained GAN model. The fourth and the last panel is the difference between the ground truth and the predicted image in the  $(u, v)$  plane. The uniform background color in the difference panel suggests that the network is picking up white noise from the  $(u, v)$  plane.

For instance, the TensorFlow tutorials<sup>6</sup> demonstrate its application to a dataset of architectural facades. However, to adapt the pix2pix GAN This architecture has been adapted for the phase retrieval problem, some modifications are necessary at hand here. The network is implemented using the TensorFlow library (?), calculations are performed with scipy (?), and plots are generated with matplotlib (?).

### 5.3. Hyperparameter Tuning

The GAN-cGAN model architecture used in this work depends on several parameters employs several hyper-parameters, which are explained briefly below (for a more in-depth discussion, see ?).

The learning rate (*lr*) of the optimizer determines how much the model updates its parameters with each iteration. A learning rate that is too small may lead to underfitting, while one that is too large can render the model unstable. Therefore, selecting an appropriate learning rate is crucial (?). Fig. ?? illustrates the effect of different learning rates on both the Generator and Discriminator losses. As expected, lower learning rates are typically trained with the same number of steps adopted the strategy of training both the networks with equal preference (Discriminator repetition = 1).

The kernel size refers to the dimensions of the convolutional kernel used in the network, determining how many pixels are combined to produce a new pixel. A larger kernel size can capture features spanning several pixels, but it may also incorporate unrelated features. As shown in Fig. ??, the kernel size does not have a significant impact on the loss functions; however, smaller kernel sizes tend to lead to a slight rise in the Generator loss. In training our model, we did not notice any significant advantage derived from this strategy. Since the generated images do not noticeably improve with additional Discriminator training, both networks are typically trained with the same number of steps adopted the strategy of training both the networks with equal preference (Discriminator repetition = 1).

The amount of noise is controlled by two parameters, “alpha” and “beta”, which indicate the percentage of pixels altered to either white or black—, hence the term Salt and Pepper noise. Here, “alpha” is applied to the real image, while “beta” is applied to the generated image. Different ratios (“alpha/beta”) can lead to varying model performance; however, our results indicate that distinct noise rates do not significantly affect the loss functions. Figure ?? shows the loss functions for smaller images (64 × 64).

The batch size defines the number of images processed simultaneously by the network. Smaller batch sizes have been observed to improve generalization (?). As illustrated in Fig. ??, processing two images at once results in fewer outliers. However,

789 ing time, a batch size of 1 is used. Besides, in Pix2Pix  
790 cGAN implementations found in literature this choice  
791 is found to be often preferred.

5pt When training, The buffer size of a Pix2Pix GAN  
792 refers to a small memory of image pool of previously  
793 generated images. They are occasionally fed to the  
794 Discriminator in place of the freshly generated ones.  
795 This strategy of mixing old and new fakes mitigates the  
796 risk of mode collapse wherein the Discriminator tends to  
797 map all or large number of generated images to only one  
798 or a few real “ground truth” image(s). We have chosen  
799 a fairly large buffer size (=1400) to protect the model  
800 against mode collapse.

In the training of GANs, one often-followed strategy to potentially boost performance is to give the Discriminator an advantage by increasing its number of training steps before returning to the Generator’s training. This hyperparameter is referred to as the Discriminator repetition (as seen in Table 1). While this can lower the Discriminator loss as shown in Fig. 7, it also increases training time and leads to a slight rise in the Generator loss. In training our model, we did not notice any significant advantage derived from this strategy. Since the generated images do not noticeably improve with additional Discriminator training, both networks are typically trained with the same number of steps adopted the strategy of training both the networks with equal preference (Discriminator repetition = 1).

5pt Finally, the One domain specific hyperparameter of the cGAN model presented here is the Number of Telescopes  $N_T$ . The degree of sparse sampling of the intensity interferometric (II) image plane can be varied to provide the model with access to more pixels. Increasing the number of telescopes results in more baseline of active (non-zero) pixels. Point to note here, is that the coverage of the Fourier interferometric plane (number of active pixels in the II image) scales with available number of baselines, and the latter scales quadratically with the number of telescopes. Fig. 8 shows the loss functions for different numbers of telescopes. There is a significant disparity in performance, partly because the relationship between telescopes and baselines is non-linear and due to the negligible input, this analysis was not repeated. The Generator and Discriminator exhibit less smooth training, as indicated by the loss functions being non-smooth. Overall, the degree of sparse sampling appears to have the most pronounced effect of all the hyperparameters.

## 6. IMAGES RECONSTRUCTED BY THE GAN

5pt In this section, we begin by discussing phase retrieval using hyperparameter Output Channels refers to the

<sup>6</sup> <https://www.tensorflow.org/tutorials/generative/pix2pix>

number of channels in the generator output (e.g., 1 is used, and equal training is provided to for grayscale, 3 for RGB). It is worthwhile to recall that the cGAN model constructed in this work is trained on “ground truth” target images and the simulated II data, both in grey scales as seen in Fig.5. It is natural that the output of this model will be in grey scales only. Therefore the value of this hyperparameter is set to 1. The choice of hyperparameter  $\lambda$  has been commented upon earlier.

An optimized set of hyperparameters is selected through an iterative process of training and validation. For a tentatively chosen set of the hyperparameters, the model is trained using the Training Set until the both the Discriminator and the Generator loss functions are minimized. This model, thus trained along with its model parameters, is then passed through validation using the Validation Set. This cycle of training and validation is iterated till an optimal set of hyperparameters is arrived at. During each epoch of training of the model, both the Discriminator and the Generator .

### 5.1. Predicted Image from the Trained GAN

Fig. 9 demonstrates the success of the GAN in training a. The GAN is trained for 100,000 steps and subsequently tested on various validation datasets to produce predicted images of the stars. In Fig. 9, four panels from left to right in each row illustrate the performance of the GAN in reconstructing the stars' shape, size, and brightness distribution using II images of a sample of the fictitious fast-rotators drawn from the Testing Set. The four panels from left to right in each row of Fig. 9 represent the following:

The Pix2Pix cGAN architecture along with the choice of the values of the hyperparameters mentioned in the Table -1 and used in the implementation of this architecture constitutes the cGAN model (hereinafter referred to as “the GAN Model” or simply “the Model”).

## 6. IMAGE RECONSTRUCTION: RESULTS AND EVALUATION

**Table 1.** Selected hyperparameters used for training the model.

Hyperparameter	Value
Learning rate	2e-4
Kernel size	5
Alpha/Beta	1
Batch size	1
Buffer Size	1400
Discriminator repetition	1
Number of Telescopes	4
Output Channels	1
Lambda	100

In this section, we examine the performance of the GAN Model whose architecture and choice of hyperparameters have been discussed above. We subject the trained Model to the task of phase retrieval and image reconstruction on the Testing Dataset.

### 6.1. Visual Evaluation of Images Predicted by the Model

Fig. 9, four panels from left to right in each row illustrate the performance of the GAN in reconstructing the stars' shape, size, and brightness distribution using II images of a sample of the fictitious fast-rotators drawn from the Testing Set.

The four panels from left to right in each row of Fig. 9 represent the following:

- The left panel represents the sparse II pattern obtained by the simulated observation using the four IACTs illustrated in Fig.1. As explained earlier, this image acts as part of the input, namely its “condition” part. This image acts as the condition that the sky-images of the star generated by the Generator must conform to.
- The second panel from left displays the real image, or ground truth target image, which the Discriminator loss function uses to distinguish from the images generated by the Generator.
- The third panel from left presents the reconstructed (or predicted) image corresponding to the ground truth (second panel) and generated by the trained Model. The similarity of these two images indicates the success of the Model in its stated objective of image reconstruction. We remark that rotating the images by 180° would not change the data. That is, each predicted image contains an arbitrary choice among two possible orientations, differing by 180°.

- 926 • The right panel shows the residuals between the  
 927 ground truth target image and the predicted image  
 928 in the interferometric plane. The small values are  
 929 indicative of the success of training the Model.

930 The predicted images ~~in and the residuals presented~~  
 931 ~~in the third and the fourth columns (from left) of Fig. 9~~  
 932 ~~yield show~~ encouraging results, ~~accurately~~ conveying  
 933 visual information about the source's size, shape,  
 934 and brightness distribution across its surface ~~fairly~~  
 935 ~~accurately. This has been achieved on the basis~~  
 936 ~~of the input provided by II observation using only~~  
 937 ~~six baselines. However, further improvements can,~~  
 938 ~~corresponding to four telescopes, at present the~~  
 939 ~~maximum on which II is already implemented. Further~~  
 940 ~~improvements could surely be achieved by increasing~~  
 941 ~~the number of telescopes to maximize enhance the~~  
 942 ~~coverage of the ( $u, v$ ) plane, making. A closer examination~~  
 943 ~~of this proposition might be able to contribute to the~~  
 944 ~~design and instrumentation aspects in the existing and~~  
 945 ~~upcoming CTAO an ideal candidate for this approach.~~

## 6.2. Evaluation of *GAN* the Model using Moments

947 The reconstructed images are visually compelling,  
 948 demonstrating the *GAN*Model's effectiveness in us-  
 949 ing II to reconstruct images. However, visual as-  
 950 sessment alone is insufficient; statistical evaluation ~~of~~  
 951 ~~the generated images in comparison with the ground~~  
 952 ~~truth images~~ is necessary to validate the results.  
 953 ~~To achieve this, we employ image moments as a statistical method.~~ We  
 954 ~~present here the results of our calculation and~~  
 955 ~~comparison of the moments of distribution pixel~~  
 956 ~~brightness in the target "Ground Truth" images and~~  
 957 ~~the "Predicted" images.~~

958 Image moments capture key properties of the re-  
 959 constructed objects— such as shape, size, and  
 960 intensity distribution— by quantifying features  
 961 like position, orientation, and brightness distri-  
 962 bution. By comparing the moments of the  
 963 ~~GAN-generated images to Model-generated images~~  
 964 ~~with~~ those of the ground truth, we can objectively  
 965 assess the consistency and accuracy of the reconstruc-  
 966 tion. This approach provides a reliable framework for  
 967 evaluating reconstruction quality, as image moments  
 968 can reveal subtle differences in geometric and intensity  
 969 properties that might not be apparent through visual  
 970 inspection alone.

971 The raw moment  $M_{ij}$  of an image is defined as (?)

$$972 M_{ij} = \sum_x \sum_y x^i y^j I(x, y) \quad (17)$$

973 where  $I(x, y)$  represents the intensity at pixel  $(x, y)$ .  
 974 The zeroth order raw moment, or monopole, represents

975 the total intensity of an image. It is computed by sum-  
 976 ming all pixel values across the image, yielding an over-  
 977 all intensity measure. In this context, analyzing the  
 978 monopole provides the total ~~flux of fast-rotating pixel~~  
 979 ~~brightness of the images of the fictitious stars. According~~  
 980 ~~to Eq. (17), the monopole of an image is calculated~~  
 981 ~~as:~~

$$982 M_{00} = \sum_x \sum_y I(x, y). \quad (18)$$

### The left figure-

983 An ideally trained Model should predict the  
 984 overall pixel brightness of the generated images  
 985 to be in the same range of values, if not equal  
 986 to those of the ground truth images. The left  
 987 panel of Fig. 10 displays the monopole values  
 988 for 50–100 reconstructed images. The plot re-  
 989 veals a ~~linear relationship between the monopole broad~~  
 990 ~~agreement in the overall intensity~~ of the ground truth  
 991 ~~(real image) on the x-axis and that of targets and the~~  
 992 ~~predicted (reconstructed) image on the y-axis, consistent across sou~~  
 993 ~~images. However, a slightly higher brightness of~~  
 994 ~~reconstructed images in the intermediate range of~~  
 995 ~~brightness is evident. This could, perhaps, be mitigated~~  
 996 ~~by tuning the Batch Size hyperparameter.~~

997 While the monopole effectively represents the total  
 998 brightness, it does not provide information about the  
 999 position, shape, size, or detailed brightness distribution  
 1000 of the fast-rotating stars. For these aspects, higher-order  
 1001 moments are necessary.

1002 The ~~center of mass of the sky image of any stellar object, is deter~~  
 1003 ~~order raw moments normalized by the respective~~  
 1004 ~~monopole moments of the images given by~~

$$1006 x_c = \frac{M_{10}}{M_{00}} = \frac{\sum_{x,y} x \cdot I(x, y)}{\sum_{x,y} I(x, y)} \\ 1007 y_c = \frac{M_{01}}{M_{00}} = \frac{\sum_{x,y} y \cdot I(x, y)}{\sum_{x,y} I(x, y)} \quad (19)$$

1008 Here,  $I(x, y)$  represents the intensity at pixel  $(x, y)$ ,  $M_{00}$  is the monopole of the image,  $x_c$  and  $y_c$  represent the centroids  $(x_c, y_c)$  of the pixel brightness distribution of the images. An ideally trained GAN model should produce the centroids of the target and predicted images within a small range of pixels. A larger range would imply a low fidelity in learning the brightness distribution of ground truth images. The middle and right ~~panel~~ panels of Fig. 10 compare the centroids  $(x_c, y_c)$  of 50–100 predicted images with their corresponding ground truths respectively. ~~The~~ We notice that the coordinates of the centroids of ground truth images are spread across a range of 2 pixels whereas the those of the predicted images are spread across a span of 4 pixels along  $x$ -axis and 7 pixels along  $y$ -axis. This clustering of

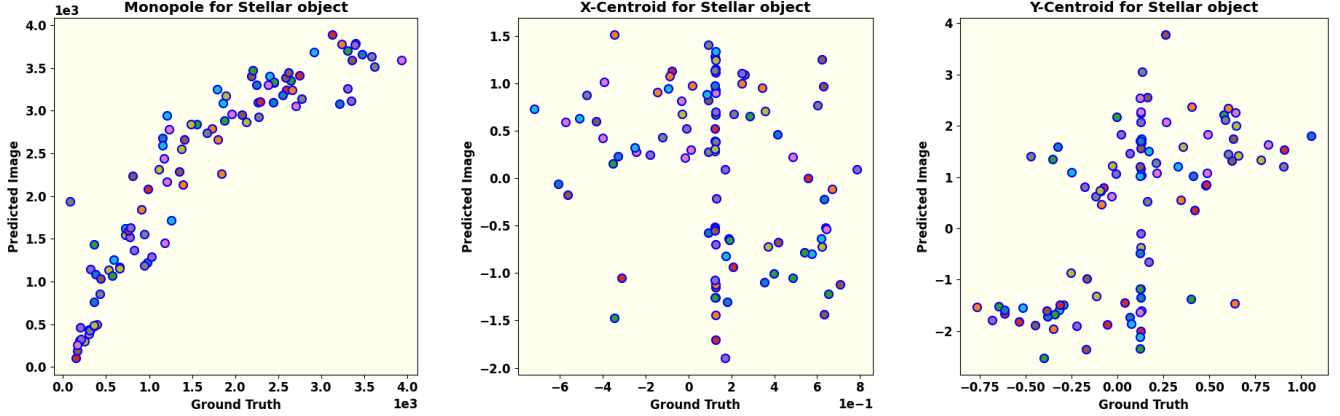


**Figure 10.** This set of figures shows comparisons of the comparison monopole, and the coordinates of the centroids ( $x_c, y_c$ ) of the pixel brightness distribution of the ground truth images and the corresponding images predicted (generated) by the trained model. The monopole moment of the images represents the overall pixel brightness of the images. The values,  $x$ -centroid as expected of a trained Model, not only lie in same range, but lie close to the diagonal and  $y$ -centroid for show an approximate equality. The centroids of both the ground truth images and the predicted images generated by lie within small ranges of pixel values as should be expected of an ideally trained GAN model. Please see the relevant text for detailed comments.

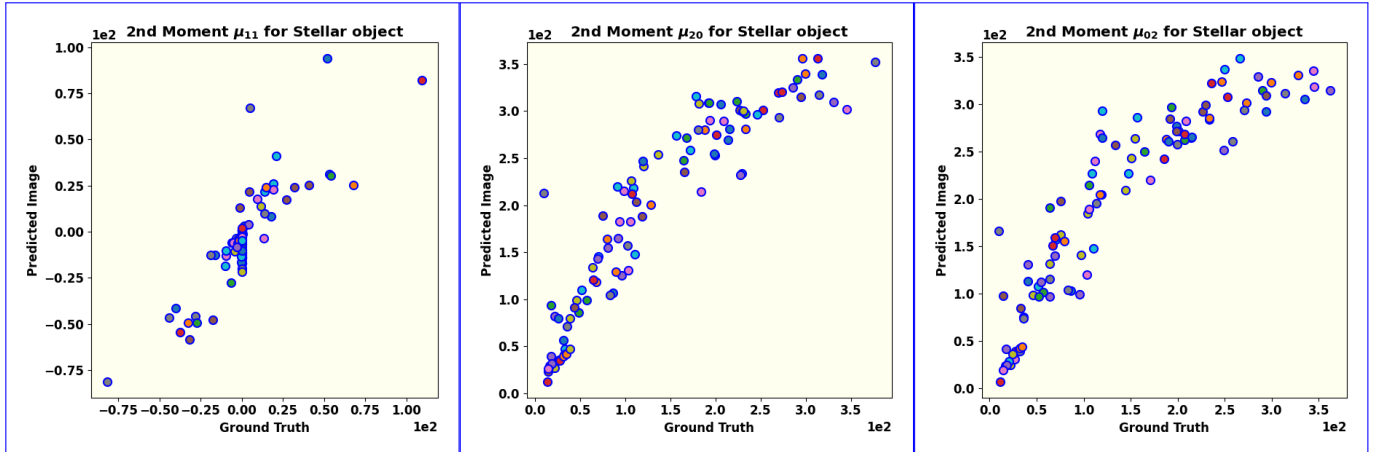


**Figure 11.** The second order central moment of the brightness distribution of the images is analogous to the moment of inertia of a mass distribution. The panels of this figure show the comparison of the second order moments ( $\mu_{11}, \mu_{20}$ , and  $\mu_{02}$ ) of the predicted images vs. the ground truth images from left to right respectively. Approximate equality of these moments is evident. The small scatter in the moments of the predicted images is indicative of a balanced training of the Model.

centroids within a specific small scale range across all results indicates that the reconstructed images accurately represent the spatial location of the fast-rotating star have large offsets.

The second-order central moments provide information about the size and shape of stellar objects. Shown here are all the third-order central moments for  $p+q=2$ . Furthermore, these calculated centroids are instrumental in analyzing the shape, size, and brightness distribution of the stars using higher-order image moments. To this end, the central moment of an image is calculated according to:

$$\mu_{pq} = \frac{1}{M_{00}} \sum_x \sum_y (x - x_c)^p (y - y_c)^q I(x, y). \quad (20)$$

The sum of  $p$  and  $q$  defines the order of the central moment.

The second-order central moment of the brightness distribution of the images is analogous to the moment of inertia of a mass distribution. Fig. 11 presents the comparison of second-order central moments.

$(\mu_{11}, \mu_{20}, \mu_{02})$ , which are used to study the structure of a fast-rotating star along the line of sight (as explained in the upcoming subsection). All three plots demonstrate a linear relationship in the second-order moments, similar to the monopole, thereby confirming the success of applying the GAN Model to reconstruct images with II.

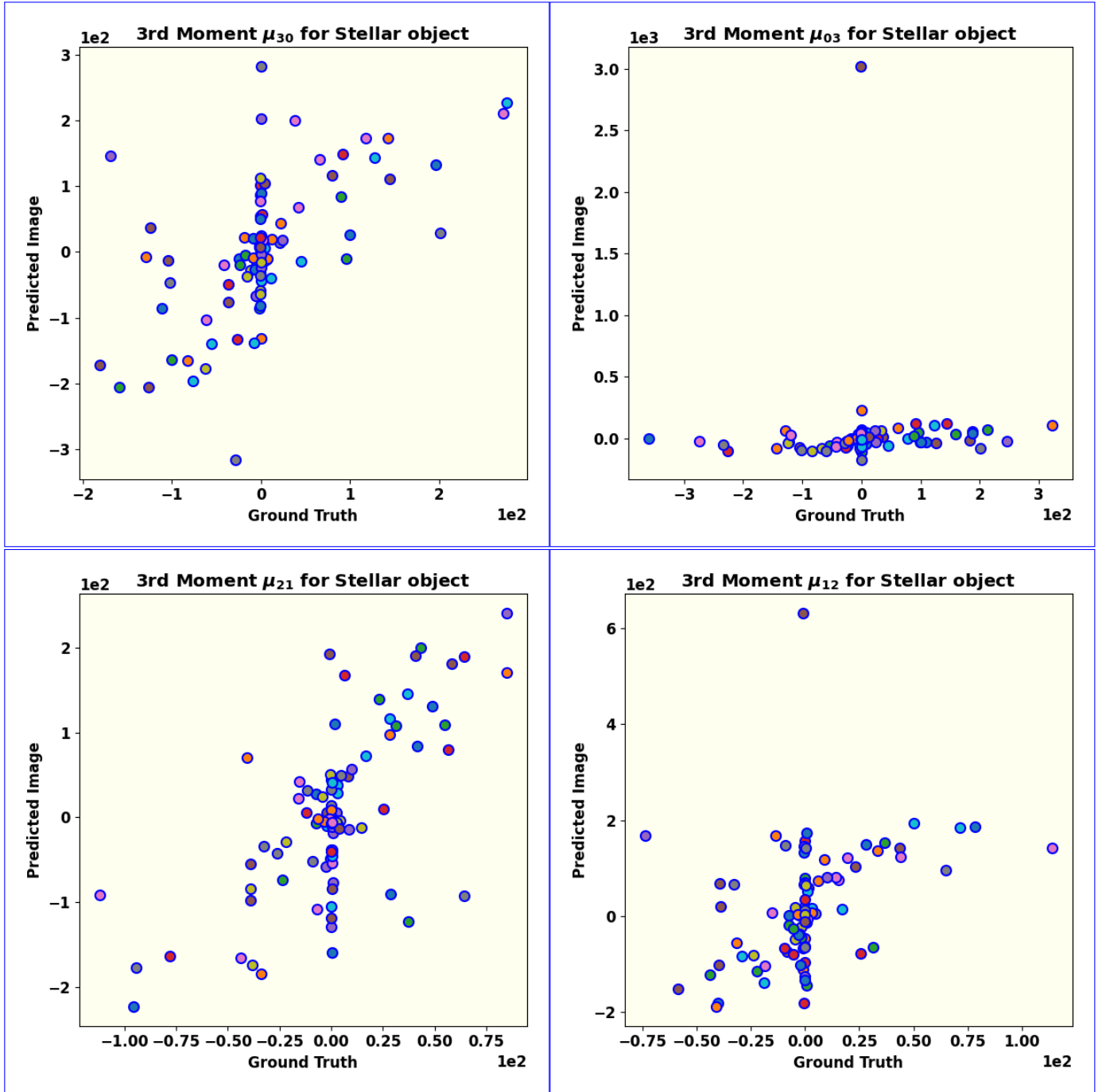


**Figure 12.** Shown here are all the third-order central moments ( $\mu_{30}$ ,  $\mu_{03}$ ,  $\mu_{21}$ , and  $\mu_{12}$ ) for ground truth and predicted images generated by the trained Model. They represent the skewness of the brightness distributions. The low skewness in the brightness distribution of the ground truth images is evident. One outlier among the predicted images dominates their skewness distribution along the  $y$ -axis as seen in the values of  $\mu_{03}$  and  $\mu_{12}$ . The trained Model, however, seems to have learned the approximately uniform distribution of skewness along the  $x$ -axis as is evident, with a few outliers though, in the values of  $\mu_{30}$  and  $\mu_{21}$ .

1048 5pt The brightness distribution is characterized by the skewness of the image, which is quantified by calculating the  
 1049 small scatter in the moments of the predicted images.  
 1050 indicates robust learning of the Model without  
 1051 over-fitting.

1052 The third-order central moments ( $\mu_{30}, \mu_{03}, \mu_{21}, \mu_{12}$ )  
 1053 of the images quantify the degree and direction of  
 1054 asymmetry of the brightness distribution around their  
 1055 respective centroids. Fig. 12 presents a comparison of all  
 1056 third-order moments for both the ground truth and the  
 1057 reconstructed image. The skewness along the  $x$ - and All  
 1058 the four panels show a low skewness in the brightness  
 1059 distribution of the ground truth images. The skewness  
 1060 of the predicted images along the  $y$ -axes ( $\mu_{30}$  and  $\mu_{12}$ )  
 1061 is dominated by one outlier as seen in the values of  $\mu_{03}$   
 1062 ) appears acceptable, as shown in both upper panel of Fig. 12,  
 1063 where a linear relationship exists between the ground truth and  
 1064  $\mu_{12}$ —particularly  $\mu_{12}$ , as depicted in both lower panel of Fig. 12,  
 1065 do not align as well. This indicates that further improvement  
 1066 However, the approximately uniform distribution of  
 1067 skewness of the predicted images along the  $x$ -axis, with  
 1068 a few outliers though, as seen in the values of  $\mu_{30}$  and  
 1069  $\mu_{21}$  suggests that this feature in the ground truth images  
 1070 has been picked up fairly well during the training of the  
 1071 Model.

### 1070 6.3. The reconstructed Parameters for object

1071 The centroids ( $x_c, y_c$ ) indicate only the center of the  
 1072 star and its spatial location in the image. In contrast,  
 1073 the second-order central moments determine the orien-  
 1074 tation, semi-major axis, and eccentricity relative to the  
 1075 source's center (?). These moment-based parameters  
 1076 fully describe the two-dimensional ellipse that fits the  
 1077 image data.

1078 The orientation of a fast-rotating star along the line of  
 1079 sight is defined in terms of second-order central moments  
 1080 as

$$1081 \theta = \frac{1}{2} \arctan \left( \frac{2\mu_{11}}{\mu_{20} - \mu_{02}} \right). \quad (21)$$

1082 The semi-major and semi-minor axes of the stellar ob-  
 1083 ject are computed using the second-order central mo-  
 1084 ments and are denoted as  $a$  and  $b$ , respectively.

$$1085 a = 2\sqrt{mp + \delta} \\ 1086 b = 2\sqrt{mp - \delta} \quad (22)$$

1087 where,

$$1088 mp = \frac{\mu_{20} + \mu_{02}}{2} \quad (23)$$

1089 and

$$1090 \delta = \frac{\sqrt{4\mu_{11}^2 + (\mu_{20} - \mu_{02})^2}}{2}. \quad (24)$$

1091 Using the calculated axis values, the eccentricity of the  
 1092 fast-rotating star is determined as:

$$1093 e = \sqrt{1 - a/b}. \quad (25)$$

1093 Eqs. 21-25 describe the elliptical nature of the stellar The  
 1094 object (in this case, a fast-rotating star) and provide in-  
 1095 formation on its shape and size, depending on the com-  
 1096 puted values. In contrast, the brightness distribution  
 1097 is characterized by skewness, which is quantified using  
 1098 third and higher-order moments.

## 1099 7. CONCLUSION

1100 Intensity Interferometry (II) is re-emerging as a  
 1101 promising technique to overcome the challenges of very  
 1102 long baseline interferometry in the optical wavelength  
 1103 range. However, compared to radio-interferometry, op-  
 1104 tical interferometry faces an important a major hurdle:  
 1105 photon correlation captures only the magnitude of the  
 1106 interferometric signal, resulting in a loss of phase infor-  
 1107 mation.

1108 This work addresses the challenge of phase re-  
 1109 trieval in II using a machine-learning technique,  
 1110 specifically a conditional Generative Adversarial  
 1111 Network (cGAN). Our study demonstrates that  
 1112 applying a cGAN to II data successfully recovers the  
 1113 size, shape, and brightness distribution of  
 1114 a fast-rotating star. Evaluations based on image moments—specific  
 1115 rotating stars can be recovered by a Pix2Pix cGAN  
 1116 model trained on the combined input of the sky-image  
 1117 of known sources along with their respective II data.  
 1118 In this training the sky-image acts as the real “ground  
 1119 truth” and the II data acts as the “condition”. The  
 1120 Discriminator of our Model is trained to efficiently  
 1121 distinguish between the real images and fake (generated)  
 1122 images based on the “ground truth” images and the  
 1123 respective II data as the condition. The Generator is  
 1124 trained to generate progressively realistic images which  
 1125 are also consistent with the condition of the II data. The  
 1126 evaluation of the trained Model is then carried out by  
 1127 comparison of image moments of ground truth images  
 1128 and generated images. Specifically, the monopole, sec-  
 1129 ond, and third-order moments are compared. The  
 1130 results support the effectiveness of cGAN in achieving  
 1131 accurate image reconstruction from a simulation of II from a single  
 1132 stated objective.

1133 While the results of this study highlight the significant  
 1134 potential of machine learning, and in particular the ap-  
 1135 plicability of cGAN, for image reconstruction in II, sev-  
 1136 eral aspects require further refinement. First, an impor-  
 1137 tant factor in the reconstruction process is the extent of  
 1138 Fourier plane coverage, which depends on the number of  
 1139 available telescopes and the total observing time. The  
 1140 reasonable success of this piece of work suggests that a  
 1141 network of higher number of telescopes providing higher  
 1142 number of baselines and greater coverage of the  $(u, v)$   
 1143 plane signal, would play a critical role in projects of im-

age reconstruction of more complicated stellar systems can be undertaken. Future work might explore different observatory layouts to assess their impact on image reconstruction quality. Second, detector efficiencies, which impact the signal-to-noise ratio (SNR) of actual observational data, have not yet been incorporated; addressing these factors will be crucial for more accurate SNR estimation. Third, exploring and comparing alternative methods for image generation could reveal approaches that outperform cGAN in reconstructing stellar images with II. Fourth, experimenting with different loss functions could provide additional insights into the reconstruction quality. Although further testing is needed to refine the GAN and enhance its robustness and reliability, our findings suggest that machine learning is a promising approach for phase reconstruction in II.

1144  
1145  
1146  
1147  
1148  
1149  
1150  
1151  
1152  
1153  
1154  
1155  
1156  
1157  
1158  
1159

## NOTE ON SOFTWARE

The code used for this work is available on the DOI:  
[10.5281/zenodo.17598807](https://doi.org/10.5281/zenodo.17598807)

1160  
1161  
1162  
1163  
1164  
1165  
1166  
1167  
1168  
1169

## ACKNOWLEDGEMENTS

**Acknowledgment:** One of the authors (SS) gratefully acknowledges the computing facilities and the local hospitality extended to him by the Inter-University Centre for Astronomy and Astrophysics (IUCAA), Pune, India under its Visiting Associate Programme during the preparation [and finalization](#) of this manuscript.

## REFERENCES

- 1170 Abadi et al., M. 2016, arXiv preprint arXiv:1603.04467  
 1171 Abe et al., S. 2024, MNRAS, 529, 4387  
 1172 Acciari et al., V. A. 2020, MNRAS, 491, 1540  
 1173 Acharyya et al., A. 2024, The Astrophysical Journal, 966, 28  
 1174  
 1175 Aleksic et al., J. 2016, Astroparticle Physics, 72, 76  
 1176 Archer, A., Aufdenberg, J. P., Bangale, P., et al. 2025, arXiv e-prints, arXiv:2506.15027, doi: [10.48550/arXiv.2506.15027](https://doi.org/10.48550/arXiv.2506.15027)  
 1177 Baumgartner et al., S. 2020, MNRAS, 498, 4577  
 1178 Cocomini et al., D. 2021, arXiv preprint arXiv:2122.11578  
 1179 Dravins et al., D. 2013, Astroparticle Physics, 43, 331, doi: [10.1016/j.astropartphys.2012.04.017](https://doi.org/10.1016/j.astropartphys.2012.04.017)  
 1180 Fienup, J. 1982, Applied Optics, 21, 2758  
 1181 Gamo, H. 1963, Journal of Applied Physics, 34, 875  
 1182 Gerchberg, R. W. 1972, Optik, 35, 237  
 1183 Glauber, R. J. 1963, Physical Review, 130, 2529  
 1184 Goldberger et al., M. L. 1963, Physical Review, 132, 2764  
 1185 Goodfellow et al., I. 2014, Advances in neural information processing systems, 27  
 1186 Hanbury Brown, R., & Twiss, R. Q. 1956, Nature, 178, 1046  
 1187 Hanbury Brown et al., R. 1954, The London, Edinburgh, and Dublin Philosophical Magazine and Journal of Science, 45, 663  
 1188 Hanbury Brown et al., R. 1957, Proceedings of the Royal Society of London. Series A. Mathematical and Physical Sciences, 242, 300  
 1189 Hanbury Brown et al., R. 1958, Proceedings of the Royal Society of London. Series A. Mathematical and Physical Sciences, 243, 291  
 1190 Hanbury Brown et al., R. 1974, Monthly Notices of the Royal Astronomical Society, 167, 121  
 1191  
 1192  
 1193  
 1194  
 1195  
 1196  
 1197  
 1198  
 1199  
 1200  
 1201
- 1202 Hecht, E. 2002, Optics (Addison Wesley)  
 1203 Holmes et al., R. 2010, in Adaptive Coded Aperture Imaging, Non-Imaging, and Unconventional Imaging Sensor Systems II, Vol. 7818, SPIE, 175–185  
 1204  
 1205  
 1206 Hu, M.-K. 1962, IRE transactions on information theory, 8, 179  
 1207  
 1208 Hunter, J. D. 2007, Computing in Science & Engineering, 9, 90, doi: [10.1109/MCSE.2007.55](https://doi.org/10.1109/MCSE.2007.55)  
 1209  
 1210 Isola et al., P. 2017, in Proceedings of the IEEE conference on computer vision and pattern recognition, 1125–1134  
 1211 Kirisits et al., C. 2024, arXiv preprint arXiv:2406.14143v2  
 1212 Le Bohec, S; Holder, J. 2006, The Astrophysical Journal, 649, 399  
 1213  
 1214 Leonard et al., M. 1995, Optical Coherence and Quantum Optics (Cambridge University Press)  
 1215 Li et al., X. 2014, in Imaging Spectroscopy, Telescopes and Large Optics, Vol. 9298, SPIE, 92981G1–G7  
 1216  
 1217 Lucy, L. B. 1967, Zeitschrift für Astrophysik, Vol. 65, p. 89, 65, 89  
 1218  
 1219 Lucy, L. B. 1967, Zeitschrift für Astrophysik, Vol. 65, p. 89, 65, 89  
 1220 Maeder, A. 1999, Astronomy & Astrophysics, 347, 185  
 1221 McAlister et al., H. A. 2005, The Astrophysical Journal, 628, 439  
 1222 Mirza et al., M. 2014, arXiv preprint arXiv:1411.1784  
 1223 Murphy, K. P. 2022, Probabilistic machine learning: an introduction (MIT press)  
 1224 Mustafa et al., M. 2019, Computational Astrophysics and Cosmology, 6, 1  
 1225 Nuñez et al., P. D. 2010, in Optical and Infrared Interferometry II, Vol. 7734, SPIE, 458–467  
 1226  
 1227 Nuñez et al., P. D. 2012a, Monthly Notices of the Royal Astronomical Society, 419, 172  
 1228  
 1229  
 1230  
 1231  
 1232

- 1233 Nuñez et al., P. D. 2012b, Monthly Notices of the Royal  
1234 Astronomical Society, 424, 1006
- 1235 Prince, S. J. 2023, Understanding deep learning (MIT  
1236 press)
- 1237 Rai et al., K. N. 2021, Monthly Notices of the Royal  
1238 Astronomical Society, 507, 2813,  
1239 doi: [10.1093/mnras/stab2391](https://doi.org/10.1093/mnras/stab2391)
- 1240 Rai et al., K. N. 2022, Monthly Notices of the Royal  
1241 Astronomical Society, 516, 2864,  
1242 doi: [10.1093/mnras/stac2433](https://doi.org/10.1093/mnras/stac2433)
- 1243 Ronneberger et al., O. 2015, in Medical image computing  
1244 and computer-assisted intervention—MICCAI 2015: 18th  
1245 international conference, Munich, Germany, October 5–9,  
1246 2015, proceedings, part III 18, Springer, 234–241
- 1247 Sato et al., T. 1978, Applied optics, 17, 2047
- 1248 Sato et al., T. 1979, Applied Optics, 18, 485
- 1249 Sato et al., T. 1981, Applied Optics, 20, 2055
- 1250 Schawinski et al., K. 2017, MNRAS, 467, L110
- 1251 Teague, M. R. 1980, Josa, 70, 920
- 1252 Teague, M. R. 1983, Journal of Optical Society of  
1253 America, 73, 1434
- 1254 Virtanen et al., P. 2020, Nature methods, 17, 261
- 1255 Vogel et al., N. 2025, MNRAS, 537, 2334
- 1256 Von Zeipel, H. 1924, Monthly Notices of the Royal  
1257 Astronomical Society, Vol. 84, p. 665–683, 84, 665
- 1258 Zhang et al., J. 2020, Opt. Lett., 45, 3649